Resistance law of a rod penetrating a multilayer granular raft

Zonglin Li(李宗霖), Qiang Tian(田强)†, and Haiyan Hu(胡海岩)

MOE Key Laboratory of Dynamics and Control of Flight Vehicle, School of Aerospace Engineering, Beijing Institute of Technology, Beijing 100081, *China*

(Received 16 August 2022; revised manuscript received 28 October 2022; accepted manuscript online 25 November 2022)

This paper presents an experimental study on the resistance law of a rod vertically penetrating different kinds of multilayer granular rafts with a constant velocity so as to reveal the mechanical properties of the multilayer granular rafts. The resistance was quasi-static under the chosen velocity. Experiments were conducted with different granular thicknesses, rod diameters and combinations of particles and liquids. The study shows that the resistance–displacement relation of the rod has three smooth stages. In the first stage, the resistance rapidly increased. In the second stage, the resistance curve maintained an almost constant slope. In the third stage, the resistance smoothly changed with its slope continuously increasing. Based on the corresponding physical models for each stage, the study reveals the exponential dependence of the load-bearing capacity of the multilayer granular raft on its thickness, and clarifies the capillary effects on the resistance law. The study extends the knowledge of the granular raft from monolayer to multilayer structure.

Keywords: granular matter, wet particles, saturated particles, capillary effects

PACS: 45.70.–n, 47.55.nb, 89.75.–k **DOI:** 10.1088/1674-1056/aca5ff

1. Introduction

Granular matter has many particular mechanical properties which are highly different from ordinary solids and liquids, e.g., dilatancy, jamming, anisotropy and inhomogeneity.[1–3] These important and intriguing properties are usually explored by observing the dynamic response of intruders, such as spheres,[4–7] plates[8] and rods,[9–11] during the impact or penetration into granular matter. Many empirical scaling laws[5,8,9] and analytical models[6,11] successfully predict the resistance exerted on intruders when moving into dry granule. Researches on wet particles are much more difficult than those on dry particles since the interstitial liquid will introduce cohesive forces, also known as capillary effects, which are affected by the water content, granular size and surface hydrophilicity.[12,13] These intrinsic dependences make the mechanical properties of wet particles extremely complicated.[13–16] When wet particles become saturated, the capillary effects will disappear. The buoyancy of the liquid around saturated particles attenuates the particles' gravity. In low-velocity regime, the behaviors of the saturated particles are similar to those of the dry particles under the action of an attenuated gravity.[17–19]

A granular raft is a cluster of close-packed particles at a horizontal liquid–air or liquid–liquid interface.[20,21] The granular rafts have great advantages in enhancing the load-bearing capacity of liquid interfaces,[22,23] preventing liquids from evaporation,[24] and transporting micro fluids.[25] Recent years have seen many fundamental studies to explore and improve the mechanical properties of the rafts in both horizontal[21,26–28] and vertical[22,23] directions. However, those studies mainly dealt with monolayer rafts. The mechanical properties of a multilayer raft are significantly different from those of a monolayer raft. For example, more than one layer of particles float above the liquid–air interface. Thus, it is necessary to study not only the capillarity due to the bending of the interface, but also the cohesive effects in wet particles above the interface. In addition, the buoyancy of saturated particles below the interface is larger than their gravity. As a consequence, their resultant body force has an upward direction and produces a unique internal force distribution inside the raft.

Actually, the multilayer granular raft is composed of both wet particles and saturated particles. Therefore, studying the mechanical behaviors of the multilayer granular raft under external intruders can improve the understanding of the wet and saturated granular matter. In this study, we explore the mechanical properties of the multilayer granular raft under the vertical penetration of a rod with a constant velocity. By quantitatively analyzing the resistance of the rod, this study concludes physical models of the resistance law, clarifies the capillary effects on the rod resistance, and discovers that the multilayer structure can exponentially increase the load-bearing of the granular raft. As such, the study extends the knowledge of the granular raft from monolayer to multilayer structure, and lays a foundation to further studies of multilayer rafts.

†Corresponding author. E-mail: tianqiang_hust@aliyun.com

© 2023 Chinese Physical Society and IOP Publishing Ltd

2. Experimental method

Figure 1 presents the experimental setup used to study the resistance on a rod during its vertical penetration into a multilayer granular raft with a constant velocity. During the experiment, a cylindrical polylactic acid (PLA) rod with a length of 200 mm was connected to a material testing machine (E44.104-ACBT, MTS Inc.) through a load sensor (BAB-XS-10M, 100 N) with a precision of 0.001 N and a data transmission frequency of 100 Hz. The rods with diameters $d = 20$ mm, 30 mm and 40 mm were manufactured via a 3D printer. The granular raft was composed of particles and liquids in a cylindrical acrylic container with an inner diameter of 300 mm. Granular thickness H was measured directly from the transparent container sidewall with an error of ± 2 mm. Two types of irregular plastic grains (PE and PP, short for polyethylene and polypropylene, respectively) and two types of liquids (water and saturated NaCl solution) were used. Their physical properties are listed in Table 1. The densities of the grains were smaller than those of liquids, allowing the raft to stably float on the liquid.[25–27]

Table 1. Physical properties of the particles and liquids.

Particle	PP	PE
Model number	HD5301M	M1200HS
Density ρ_g (kg/m^3)	947±15	889±18
Filling rate ϕ (%)	63.91	62.03
Repose angle θ (°)	33±1	37±1
Diameter (mm)	~3	~3
Liquid	Water	Saturated NaCl solution
Density ρ_l (kg/m^3)	1000±2	1195±3

Based on the different combinations of particles and liquids, four kinds of granular rafts, namely, PPW (PP grains and water), PEW (PE grains and water), PPN (PP grains and NaCl solution), and PEN (PE grains and NaCl solution), could be produced. The density $\rho_l - \rho_g$ of these four rafts varied from 53 kg/m^3 to 306 kg/m^3. Therefore, it was possible to study the mechanical properties of the raft under different density $\rho_l - \rho_g$.

To prepare a multilayer granular raft, the liquid and the particles were poured into the container first. Then, the top and bottom surfaces of the raft were flattened by stirring the particles and shaking the container. In order to eliminate bubbles beneath the liquid–air interface, the container sidewall was gently tapped at least for 1 minute. Afterwards, the rod was placed about 5 mm above the top of the raft in order to reach the desired velocity before touching the raft. As shown in Fig. 1(a), the rod displacement x was described by the x-position of the rod.

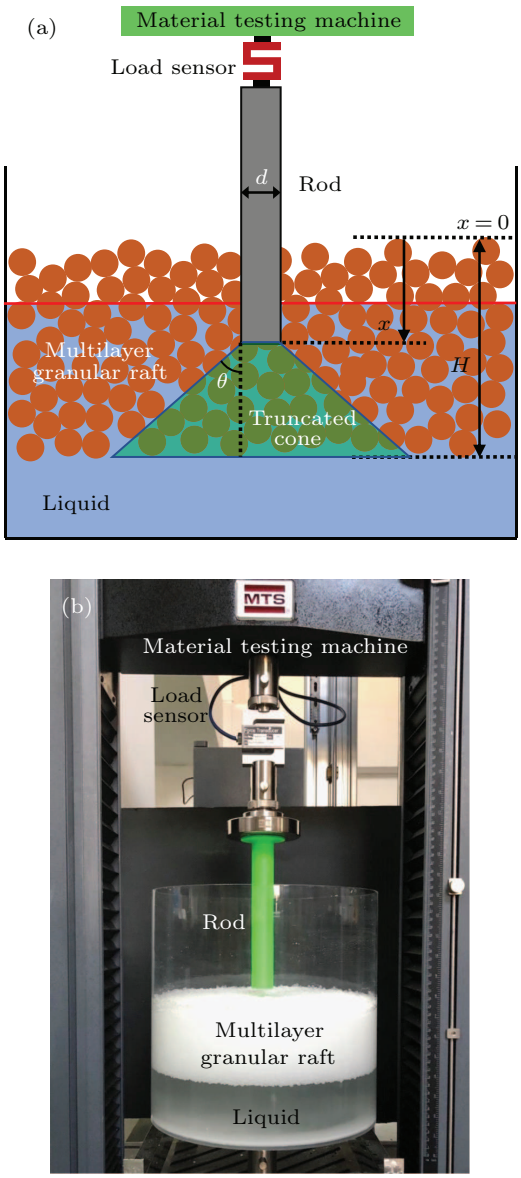


Fig. 1. (a) Sketch of the experimental setup, where the red solid line represents the liquid–air interface and the semi-transparent green area represents the truncated cone model. (b) Apparatuses of the experimental setup.

Each penetration experiment with the same experimental parameters, such as the combination of particles and liquids, the granular thickness H and the rod's diameter d, was repeated several times. In these repeated experiments, the rod was placed at the same position before moving down. However, as shown in Figs. 2(a) and 2(b), the initial contact position between the rod and the raft varied from 5 mm to 8 mm, due to the rough top surface of the raft caused by the diameter of particles (about 3 mm). Therefore, it was necessary to determine a uniform initial contact position for these repeated experiments. All raw resistance curves were averaged first. Then, the averaged resistance curve was truncated by a manually chosen threshold value ranging from 0.002–0.01 N. The initial contact position, and the zero displacement of the rod $x = 0$, were both taken as the truncated position, as shown in Figs. 2(c) and 2(d).

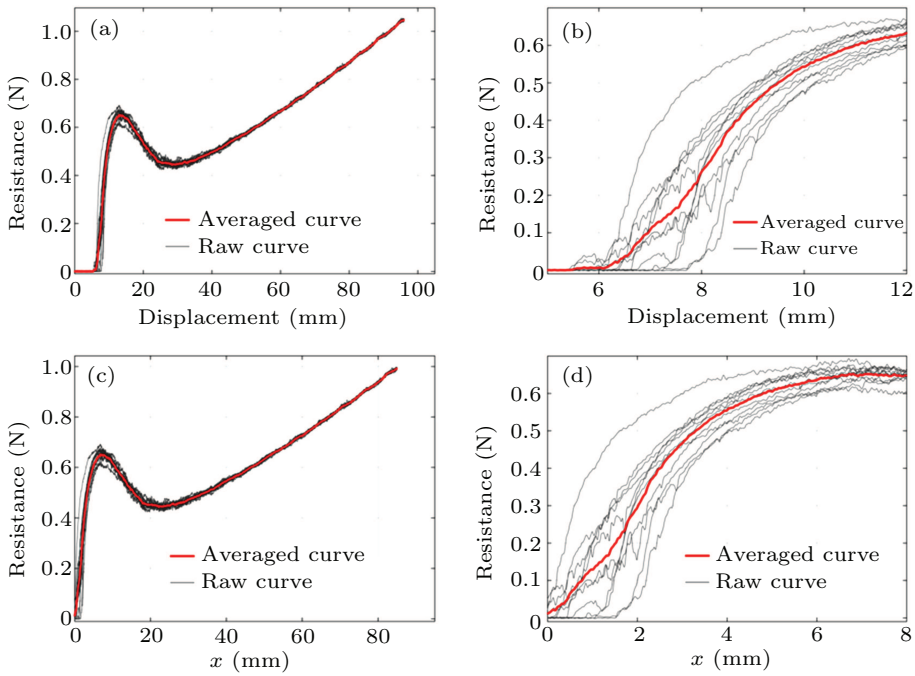


Fig. 2. The experiment, repeated 11 times, was conducted with $H = 85$ mm, $d = 40$ mm, PP particles and water. (a) The averaged resistance curve and raw resistance curves before truncation. Zero displacement represents the rod position before moving down. (b) The enlarged view of (a) in displacement 5–12 mm. (c) The averaged resistance curve and raw resistance curves after truncation. $x = 0$ represents the initial contact position. (d) The enlarged view of (c) in displacement 0–8 mm.

3. Results and discussion

3.1. Velocity-independence tests

The first step of the study is to justify the independence of the resistance on the rod velocity. For the PPW combination of particles and liquids, a rod with $d = 30$ mm penetrated into the granular raft of $H = 95$ mm with five different velocities of 5.00×10^{-4}, 8.33×10^{-4}, 1.67×10^{-3}, 3.33×10^{-3} and 5.00×10^{-3} m/s respectively, and the process was repeated twice to eliminate random errors as much as possible. As shown in Fig. 3, the averaged resistance $F(x)$ was independent of the velocity in a wide range. The experiments with other three combinations of particles and liquids, that is, PEW, PEN and PPN also maintained the similar velocity-independence relation. Therefore, the rod velocity was set to 8.33×10^{-4} m/s for other experiments discussed hereafter.

The velocity-independent resistance demonstrates the absence of the viscous resistance F^{vis} arising from Darcy's law of permeability, $F^{\text{vis}} \propto d^3\delta^{-2}v$, where v is the rod velocity, d is the rod diameter and δ is the particle diameter. In Hossain and Rognon's work,[32] F^{vis} became significant only when the velocity exceeded 4.2×10^{-4} m/s with $\delta = 0.3$ mm and $d = 40$ mm. However, the diameter of our particles was about 3 mm. As such, F^{vis} in our study should be less than 1% of Hossain and Rognon's. In other words, only if the velocity reaches about 4.2×10^{-2} m/s can we observe an obvious velocity-dependent resistance. As the first attempt to reveal the resistance law of multilayer granular rafts, the quasi-static resistance deserves to be investigated prior to the viscous resistance.

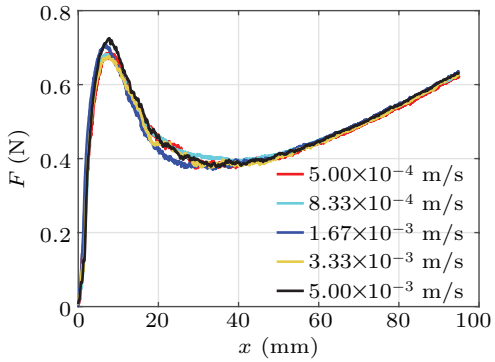


Fig. 3. The F vs. x with 5 different rod velocities in PPW experiments.

3.2. Resistance–displacement relation

As the second step of the study, the resistance law of the rod was systematically explored for different combinations of experimental parameters, including three rods with $d = 20$, 30 and 40 mm, eight rafts with $H = 25$, 35, 45, 55, 65, 75, 85 and 95 mm, and four combinations of particles and liquids, namely, PPW, PEW, PPN and PEN. The total number of combinations of parameters was $3 \times 8 \times 4 = 96$ and the number of repeated experiments was 11. As such, the total number of experiments reached 1056.

Figure 4 shows some typical averaged resistance–displacement curves, which exhibited two obvious turning points A and B no matter whether the granular layer was thick (Fig. 4(a)) or thin (Fig. 4(b)). The figure also shows that the slope of these resistance curves sharply decreased at point A, while sharply increased at point B. It is clear to see that the resistance curve had three smooth stages divided by the two turning points. This phenomenon was totally different from two

smooth stages observed for monolayer granular rafts.[22,23] In the first stage, namely stage I, the resistance rapidly increased. In the second stage, namely stage II, the resistance rapidly decreased for the thick rafts and slowly increased or decreased for the thin rafts with an almost constant slope. In the third stage, namely stage III, the resistance smoothly changed with its slope continuously increasing. The slope remained unchanged in the later period of stage III. As shown by the red line in Fig. 4(a), slight resistance fluctuations appeared in a few experiments for the thick granular raft.

Figure 5 shows x_A and x_B, that is, the x-positions of point A and point B, respectively, in experiments with PPW, PEW, PPN and PEN. Here, x_A and x_B were numerically determined by the x-positions of two corresponding maximum absolute values of the curvature of $F(x)$. The uncertainties of x_A and x_B, caused by selected smoothing parameters,[8] were ± 1 mm and ± 2 mm, respectively. Both of the averaged resistance curves (Figs. 5(a)–5(d)) and the raw resistance curves (Figs. 5(e)–5(h)) were used to calculate x_A and x_B. x_A was in 5–10 mm and not significantly affected by H, d, and different combinations of particles and liquids. In experiments with the same parameters, x_A varied within 1 mm. However, x_B was not as stable as x_A in 11 repetitions, especially when H was larger than 55 mm. Besides, x_B was linearly dependent on H. The x-position of the waterline $l_w = (1 - \rho_g/\rho_l)H$ was employed to characterize the x-position of the liquid–air interface in the absence of capillary effects (only the buoyancy was considered).

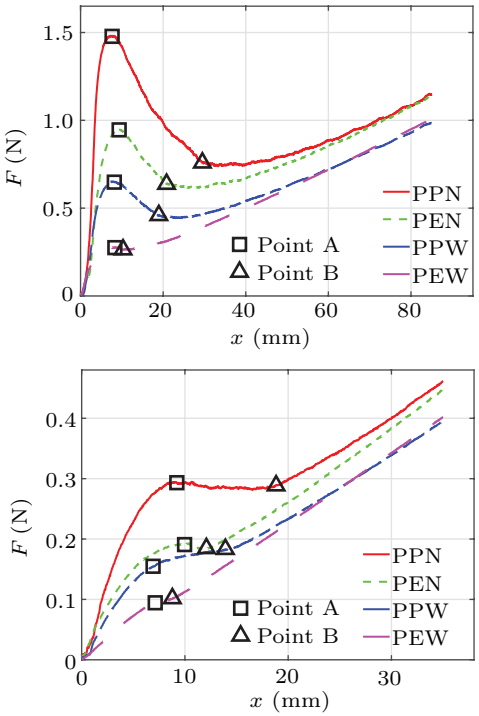


Fig. 4. The F vs. x in experiments with (a) $d = 40$ mm, $H = 85$ mm and (b) $d = 40$ mm, $H = 35$ mm.

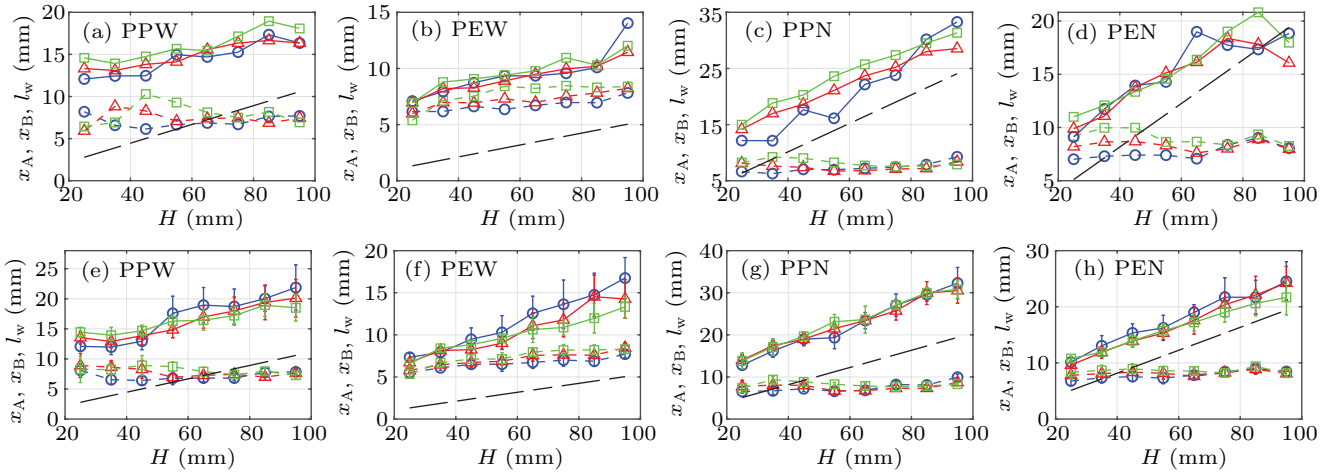


Fig. 5. The x_A, x_B and l_w in experiments with (a), (e) PPW, (b), (f) PEW, (c), (g) PPN and (d), (h) PEN. Panels (a)–(d) were calculated from the averaged resistance curves. Panels (e)–(g) were calculated from the raw resistance curves. The error bars in (e)–(h) represent corresponding standard derivation for experiments with the same parameters. The dashed lines denote x_A, the solid lines denote x_B, the black dash-dotted lines represent l_w, and the blue circles, red triangles and green squares denote different rods with $d = 20$ mm, 30 mm and 40 mm, respectively.

Specifically, capillary effects imposed the constraint on the contact angle between the liquid–air interface and the solid–liquid interface. As such, the liquid–air interface covered by particles was driven downward during the rod penetration.[20] If the capillary effects disappear, the liquid–air interface will remain horizontal and have nothing to do with the rod penetration. He *et al.*[23] penetrated a water–air interface using a rod of 12 mm and found that the interface moved down less than 2 mm before its rupture. However, when they penetrated a monolayer raft with particles' diameter of 0.79 mm using the same rod, the raft moved down nearly 5 mm before the rupture of the raft. The rupture of the interface (or the raft) suggests that the bottom of the rod was fully immersed in water.

The slopes of x_B and l_w with respect to H were obviously similar, but x_B was about 5–10 mm larger than l_w in most experiments. Therefore, a reasonable conjecture is that x_B was almost equal to the displacement of the rod as it passed across the liquid–air interface. Compared with the case of monolayer granular rafts, however, it is more difficult to directly measure

the liquid–air interface of multilayer granular rafts. Therefore, this conjecture is proved according to the resistance analysis of stage II in Subsection 3.3.2 and stage III in Subsection 3.3.3.

3.3. Physical models for resistance laws

3.3.1. Stage I

In order to derive detailed resistance laws, it is necessary to quantitatively study the resistance in those three stages. In stage I, the resistance law can be characterized via the resistance at point A, where $F_{\rm A}$ is the maximum value in stage I. Based on the experimental results, a scaling law shown in Fig. 6 is established as follows:

$$F_{\rm A} = \alpha\phi(\rho_{\rm l}-\rho_{\rm g})gd\,{\rm e}^{\beta^{-1}H}, \tag{1}$$

where α and β are fitting coefficients from the experimental results, ϕ is the filling rate and g is the gravitational acceleration. The scaling law of $F_{\rm A}$ in the averaged resistance curves is shown in Fig. 6(a), where $\alpha = (1.38\pm0.2)\times10^{-3}$ m^2 and $\beta = (3.08\pm0.2)\times10^{-2}$ m. The scaling law of $F_{\rm A}$ in the raw resistance curves is shown in Fig. 6(b), where $\alpha = (1.42\pm0.2)\times10^{-3}$ m^2 and $\beta = (3.09\pm0.2)\times10^{-2}$ m. The independence of α and β on different liquids indicates that the capillary effects had no influence on the resistance law in stage I.

In Fig. 7, the whole stage I of averaged resistance curves is normalized by using Eq. (1). The normalized curves show two different patterns. In some curves for the experiments with small H or small $\rho_{\rm l}-\rho_{\rm g}$, the normalized resistances rapidly increased in the beginning stage, and then its slope gradually decreased. In some curves for the experiments with large H or large $\rho_{\rm l}-\rho_{\rm g}$, the normalized resistances slowly increased for the first 2 mm, but then rapidly increased. The reason for this phenomenon is that the initial contact position of the rod was different in the repeated experiments, as described in Fig. 2. Large H and large $\rho_{\rm l}-\rho_{\rm g}$ both generated thick wet granular layers, which formed a rough top surface of granular rafts.

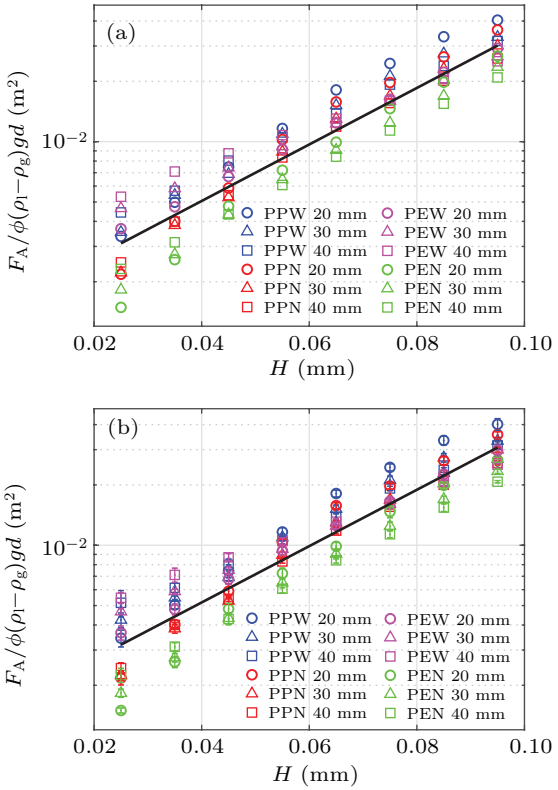


Fig. 6. The dependence of $F_{\rm A}$ on $\phi(\rho_{\rm l}-\rho_{\rm g})$, d, and H. The black solid line represents the exponential fit to the measured data. (a) The scaling of $F_{\rm A}$ for the averaged resistance curves. (b) The scaling of $F_{\rm A}$ for the raw resistance curves. The error bars represent corresponding standard derivation for experiments with the same parameters.

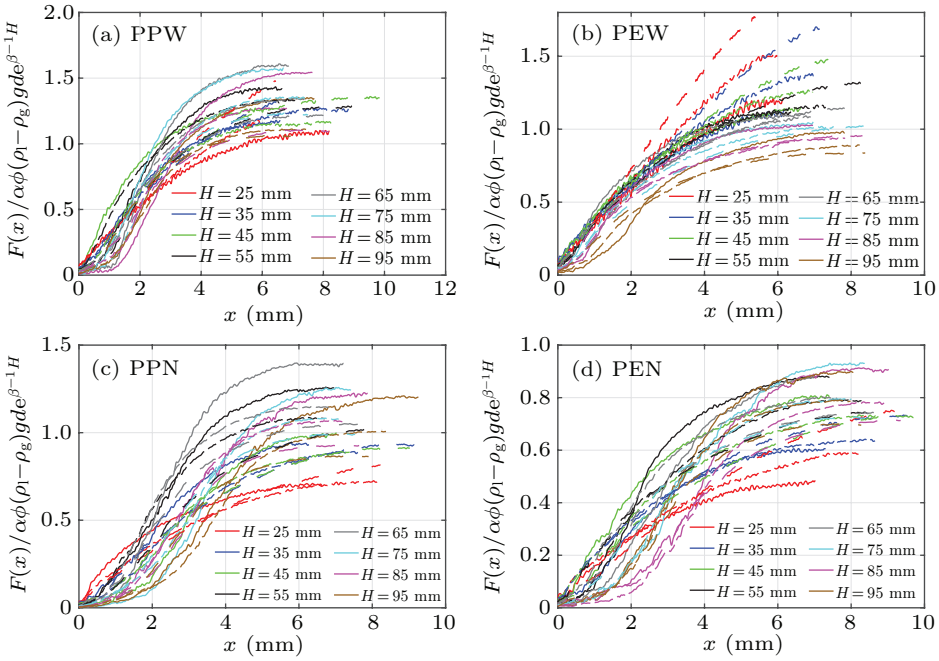


Fig. 7. The normalization of $F(x)$, $F(x)/\alpha\phi(\rho_{\rm l}-\rho_{\rm g})gd\,{\rm e}^{\beta^{-1}H}$, for the whole stage I of averaged resistance curves in experiments with (a) PPW, (b) PEW, (c) PPN and (d) PEN. The solid lines, the dash-dotted lines and the dashed lines represent experimental results with $d = 20$ mm, 30 mm and 40 mm, respectively.

Now, the study focuses on a physical model for the resistance law in stage I as follows. In this stage, the deflection of the top surface of the raft is relatively small, leading no slip among wet particles in the top of the raft. The static contact forces among these wet particles both maintain the granular raft intact and resist the rod from the penetration. Therefore, the rod resistance increases rapidly. However, once the rod approaches point A, slips may occur around particles underneath the circumference of the rod ($F_A \propto d$). Thus, the granular raft ruptures and the rod resistance fails to maintain a rapid increase. F_A can also characterize the load-bearing capacity of the raft since it is the resistance before the rapture of the raft. In addition, $F_A \propto e^H$ shows that it is possible to exponentially enhance the load-bearing capacity via simply adding particles to increase H, which cannot be achieved in a monolayer raft. Interestingly, the load-bearing capacity is not affected by capillary effects. From the above discussion, the scaling law formulated in Eq. (1) not only theoretically reveals the resistance role of the multilayer granular raft, but also estimates the load-bearing capacity of the raft.

3.3.2. Stage II

In stage II, the resistance–displacement curves were approximately straight in most experiments, but gradually deviated from a straight line with an increase of H and $\rho_l - \rho_g$ in Fig. 4. Without loss of generality, it is reasonable to introduce the averaged slope of stage II, namely, $k = (F_B - F_A)/(x_B - x_A)$, where F_B represents the resistance at point B. The averaged slope in most experiments was negative, but was positive in a few experiments with thin rafts. All of these positive slopes were smaller than their corresponding buoyancy slope, i.e., $\rho_l Sg$, where $S = \pi d^2/4$ is the bottom area of the rod. In order to eliminate the buoyancy effect, the slope could be modified as a positive variable $K = |k - \rho_l Sg|$. Then, it is possible to establish a scaling law for K as follows:

$$K = a\phi(\rho_l - \rho_g)gdH^b, \tag{2}$$

where a and b are fitting coefficients. In Fig. 8, K had a good agreement with Eq. (2) in experiments with respect to a relatively large H. However, K gradually deviated from Eq. (2) when H was relatively small, especially in PEW tests. This is because the length of stage II became relatively short if H was small or $\rho_l - \rho_g$ was small for PEW. Furthermore, K was used to determine the fitting coefficients in Eq. (2) in PEW experiments with $H \geq 65$ mm, and in PPW, PEN and PPN experiments with $H \geq 45$ mm. In Fig. 8(a), the modified slopes in the averaged resistance curves were calculated. For the experiments with water, the fitting results were $a = 31.73 \pm 1.11$ m^{1-b} and $b = 1.336 \pm 0.142$, while for experiments with NaCl solution, they were $a = 22.71 \pm 0.80$ m^{1-b} and $b = 1.394 \pm 0.175$. The bounds of these coefficients represent 95% confidence bounds. Although b did not change very much, a significantly varied for different types of liquids. This implies that K should be attributed to the capillary effects.

These modified slopes in raw resistance curves were also calculated, as shown in Fig. 8(b). The fitting results of experiments with water were $a = 21.43 \pm 0.78$ m^{1-b} and $b = 1.185 \pm 0.203$, while for experiments with NaCl solution, they were $a = 18.92 \pm 0.65$ m^{1-b} and $b = 1.328 \pm 0.169$. The error bars of the modified slope K were larger than those of F_A in Fig. 6(b), because K was affected by more parameters (x_A, x_B, F_A and F_B). The coefficient a was different between averaged curves and raw curves. This is because the coefficient b was fitted first, and then the coefficient a was calculated based on the fitted b. Actually, if b in the raw curves of water experiments had been assumed to be 1.33, then the coefficient a was equal to 30.88 ± 1.17 m^{1-b}.

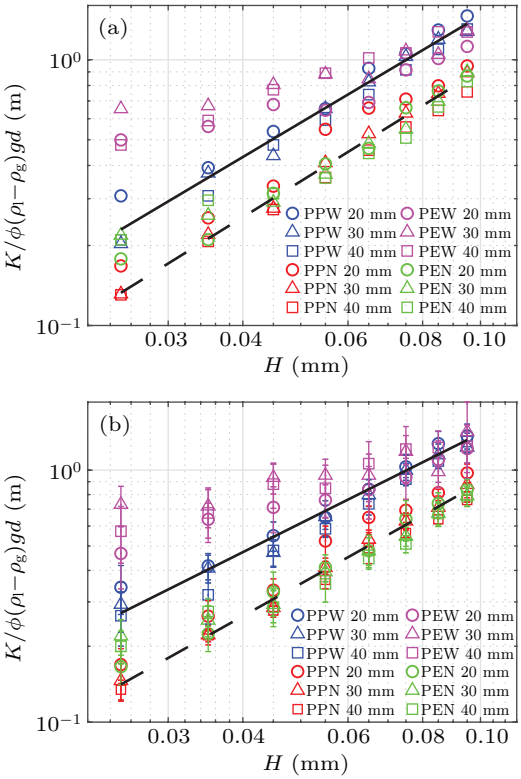


Fig. 8. The dependence of K on $\phi(\rho_l - \rho_g)$, d, and H. The black solid line represents the power fit to the data in PPW and PEW and the black dotted line represents the power fit the data in PPN and PEN. (a) The scaling of K for the averaged resistance curves. (b) The scaling of K for the original resistance curves. The error bars represent corresponding standard derivation for each group of experiments.

Now, the discussions turn to a physical model to interpret the resistance law in stage II, especially how the capillary effects contribute to the resistance. The granular raft ruptures during stage II such that wet particles beneath the intruder move downwards with the rod while other wet particles remain static. Then, slips occur at the interface between moving wet particles and static wet particles, associated with the intermittent breakages and formations of liquid bridges.[12,13] This complex slip process provides the capillary resistance, which

is linear to the rod diameter and the layer thickness of wet particles. With the downward movement of the rod, the layer of wet particles becomes thinner and thinner so that the capillary resistance linearly decreases, producing a nearly constant K in stage II. Until all wet particles underneath the rod are immersed in liquids, the capillary resistance disappears and the rod comes into stage III.

Furthermore, three issues need to be further clarified under this physical model. At first, the resistance curve in stage II may deviate from a straight line when the granular thickness H is very large. This is because the larger H leads to a longer length of stage II. The rearrangement of the saturated particles beneath the rod may significantly change the granular pressure on the bottom of the rod during the penetration in a longer stage II. This will break the linear decrease of the resistance. Second, the slope K increases with an increase of H, indicating that a thicker saturated granular layer squeezes the wet granular layer more strongly and enhances the strength of the capillary bridge force. As the coefficient b is around 1.33 and much larger than 1. This fact demonstrates that the squeeze effects in wet granular matter are quite different from the hydrostatic pressure in ordinary liquids. Therefore, the scaling $K \propto H^b$ may originate from the unique stress distribution of multilayer granular rafts. Third, the surface tension of the water is less than that of the saturated NaCl solution,[33] but coefficient a in the water is larger than that in the saturated NaCl solution. It is implausible that the strength of the capillary resistance will get larger if the surface tension of the liquid is smaller. In fact, the liquid content in wet particles may vary in different kinds of liquids. The liquid bridge force has a complicated dependence on the liquid content and the surface tension.[33] As such, the complex nature of the liquid bridge blocks the the attempt to derive an analytic relation between a and the surface tension.

3.3.3. Stage III

Finally, the study focuses on the resistance law in stage III. According to the resistance law in stage II, the capillary resistance from the slip process disappears, so that the capillary effects are not significant in this stage. To validate this, one can decompose the resultant resistance into three parts. The buoyancy from the liquids can be expressed as[35]

$$F_{\mathrm{b}}(x) = \rho_{\mathrm{l}} S g (x - l_{\mathrm{w}}). \tag{3}$$

The resistance from the particles is mainly the granular pressure on the bottom of the rod. Based on previous works,[32,36–38] a truncated cone model can describe the granular pressure as shown in Fig. 1, where the granular pressure is equal to the resultant body force of a truncated cone opening downwards from the bottom of the rod to the bottom of the granular raft, expressed as

$$F_{\mathrm{p}}(x) = f(H,d)\phi(\rho_{\mathrm{l}} - \rho_{\mathrm{g}}) S g (H - x), \tag{4}$$

where $f(H,d) = (1/3)[(1 + 2(H - x)\tan\theta/d)^2 + 2(H - x)\tan\theta/d + 2]$ represents the shape of the truncated cone. Figure 9(a) shows the comparison between the resistance $F(x)$ and the corresponding summation of the granular pressure and the buoyancy, namely, $F_{\mathrm{p}}(x) + F_{\mathrm{b}}(x)$. When $x = x_{\mathrm{b}}$, $F_{\mathrm{p}}(x) + F_{\mathrm{b}}(x)$ accurately predicts the resistance $F(x)$. But with an increase of x, $F(x)$ gradually becomes larger than $F_{\mathrm{p}}(x) + F_{\mathrm{b}}(x)$.

For further analysis, the following new variables are introduced:

$$X = (H - x)\tan\theta, \quad Y_{\mathrm{p}} = F_{\mathrm{p}}\tan\theta/(\phi(\rho_{\mathrm{l}} - \rho_{\mathrm{g}})g). \tag{5}$$

Based on Eq. (5), thus, Eq. (4) can be recast as

$$Y_{\mathrm{p}}(X) = (S/3)[(1 + 2X/d)^2 + 2X/d + 2]X. \tag{6}$$

Similarly, $F(x) - F_{\mathrm{b}}(x)$ is equivalent to

$$Y(X) = (F(X) - F_{\mathrm{b}}(X))\tan\theta/(\phi(\rho_{\mathrm{l}} - \rho_{\mathrm{g}})g). \tag{7}$$

Thus, the comparison between $Y(X)$ and $Y_{\mathrm{p}}(X)$ is equivalent to the comparison between $F(x)$ and $F_{\mathrm{p}}(x) + F_{\mathrm{b}}(x)$. Figure 9(b) shows the comparisons between $Y(X)$ and $Y_{\mathrm{p}}(X)$ for the case when $x = 45$ mm and $H \geq 45$ mm. It is clear to see that $Y(X)$ and $Y_{\mathrm{p}}(X)$ have the same trend with an increase of H, which demonstrates that the granular pressure represented by the truncated cone model successfully accounts for the trend of the rod resistance with the increase of H. However, Y was larger than Y_{p} in most experiments, which demonstrates again the existence of other resistances in stage III.

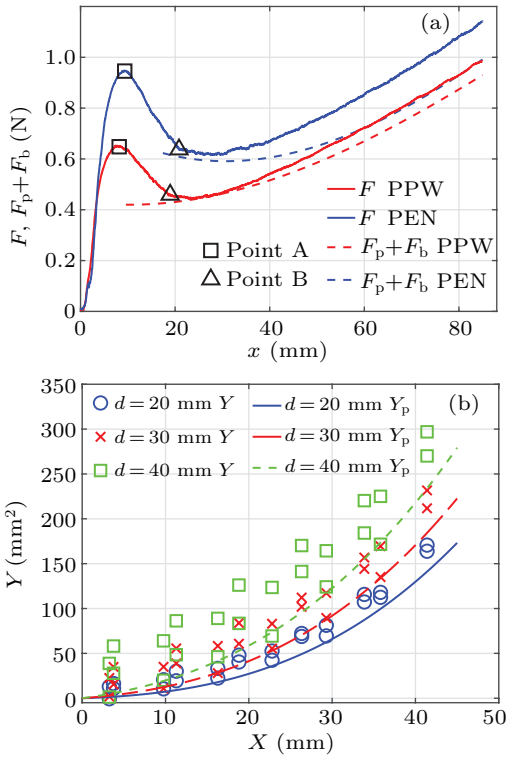


Fig. 9. (a) Two typical resistance curves and their corresponding $F_{\mathrm{p}}(x) + F_{\mathrm{b}}(x)$ in experiments with $d = 40$ mm and $H = 85$ mm. (b) The comparison between Y_{p} vs. X and Y vs. X with different rod diameter d.

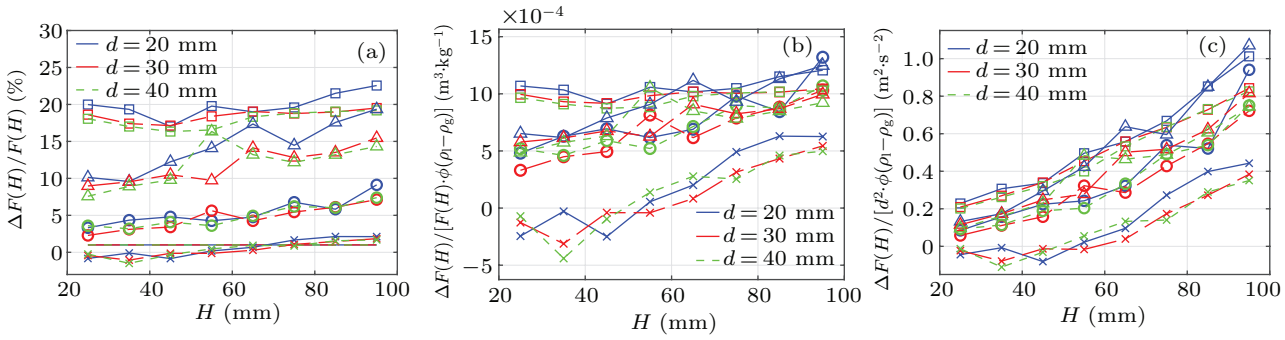


Fig. 10. (a) The $\Delta F(H)/F(H)$ vs. H. (b) $\Delta F(H)/[F(H)\cdot\phi(\rho_l-\rho_g)]$ vs. H. (c) $\Delta F/[d^2\cdot\phi(\rho_l-\rho_g)]$ vs. H. The squares, triangles, circles and crosses mark different combinations of particles and liquids: PPN, PEN, PPW, and PEW, respectively.

The results of the above quantitative analysis indicate that the summation of the granular pressure and the buoyancy can explain the resistance of the rod at point B accurately. Therefore, the capillary effects are not significant as the rod passes point B. But after point B, an additional resistance gradually arises. So the following work is to investigate the origin of the additional resistance.

The additional resistance $\Delta F(x)$ is defined by $\Delta F(x) = F(x) - F_p(x) - F_b(x)$. Figure 9(a) shows that $\Delta F(x)$ slowly increased with an increase of x and remained constant when x was close to the granular thickness H. Therefore, $\Delta F(H)$ could represent $\Delta F(x)$. As shown in Fig. 10(a), the percentage of $\Delta F(H)$ in the total resistance $F(H)$ was no more than 25%. As shown in Fig. 10(b), $\Delta F(H)/F(H)$ was linearly dependent on $\phi(\rho_l - \rho_g)$ in PPW, PEN and PPN experiments. The failure of this scaling in PEW might arise from the fact that the measurement error of ρ_g was close to $\rho_l - \rho_g$. When $x = H$, the granular pressure described by the truncated cone model turned to zero. The main resistance should be the buoyancy, which has a quadratic dependence on the rod diameter. Based on this fact, a new scaling law $\Delta F(H)/[d^2\cdot\phi(\rho_l-\rho_g)]$ is established in Fig. 10(c).

The scaling $\Delta F(H) \propto \phi(\rho_l - \rho_g)$ demonstrates that $\Delta F(x)$ mainly came from the saturated particles. Actually, two effects from saturated particles gave rise to $\Delta F(x)$. One is the granular friction due to the sidewall of the rod. The other raises from the unflatness of the bottom surface of the raft. The bottom surface humps downwards during the penetration and finally some particles even remain at the bottom of the rod, producing additional resistance, as shown in Fig. 11. With the downward penetration of the rod, these two effects became more and more significant, which coincides with the fact that $\Delta F(x)$ increases with x.

The granular friction was linear to the rod diameter, but the resistance from the bottom hump had a complex dependence on the rod diameter. Therefore, the scaling $\Delta F(H) \propto d^2$ is a coincidence that arises from the summation of these two effects.

There are some other effects that might contribute to $\Delta F(x)$. They include the measurement errors of the granular thickness H, the contact angle θ, and the granular density ρ_g. Compared with the errors caused by saturated particles, however, these errors become less significant when H gets larger. After the wet particles were pushed into the liquids, the only capillary resistance might arise from the liquid interface on the sidewall of the rod. The surface tension of saturated NaCl solution was about $\gamma = 81.75$ mN/m.[33] Let the rod diameter be $d = 40$ mm. The contact angle of NaCl solution on rod's sidewall was assumed to be 180°, so that the maximum estimation of the capillary resistance $F_c^{max} = (-\cos 180°)\cdot\pi d\gamma = 0.0103$ N. F_c^{max} was one order of magnitude less than $\Delta F(H)$ shown in the PEN experiments of Fig. 9(a). Therefore, the capillary effects were not significant in the whole stage III.

From the above analysis, the resistance F in stage III consists of three parts: F_b, buoyancy from the liquids, F_p, granular pressure represented by the truncated cone model, and ΔF, additional resistance mainly from saturated particles. The above discussions, therefore, demonstrate that the buoyancy and granular resistance from the saturated particles dominate the resistance law in stage III.

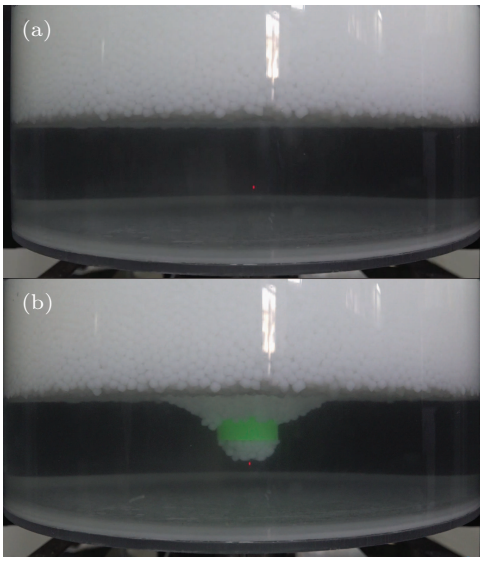


Fig. 11. Photographs of the bottom surface of the granular raft (a) before the rod penetration and (b) after the rod penetration. The red dots in the center of two photographs are the laser from the camera.

4. Conclusion

This study shows that the resistance–displacement relation of a rod penetrating a multilayer raft consists of three smooth stages. In stage I, the resistance rapidly increased. In stage II, the resistance curve maintained an almost constant slope. In stage III, the resistance smoothly changed with its slope continuously increasing. Then the study presents corresponding physical models for the resistance law in each stage.

Based on these models, the capillary effects on the resistance of the rod can be summarized. The capillary effects dominate the resistance law in stage II. They both produce the capillary resistance in stage II and drive the liquid–air interface downwards to a distance, which extends the length of stage II.

Meanwhile, the load-bearing capacity is a key property of a granular raft. Equation (1) successfully predicts this capacity and shows its exponential dependence on the thickness of the raft, which demonstrates that a multilayer granular raft can bear much more pressure than a monolayer raft. Interestingly, the load-bearing capacity is not affected by capillary effects.

Our research is the first attempt to reveal the resistance law of a rod penetrating the multilayer granular raft, and paves the way for three meaningful directions in the future. The first is to investigate the dynamic process of the hump formation during the penetration of the rod based on digital image correlation techniques. The second is to reveal how the Darcy flow mechanism contributes to the resistance when the granular raft is formed by small particles (less than 1 mm). The last is to explore the physical origin of the coefficients in Eqs. (1) and (2).

Acknowledgement

Project supported in part by the National Natural Science Foundation of China (Grant Nos. 12125201 and 11832005).

References

[1] Jaeger H M, Nagel S R and Behringer R P 1996 *Rev. Mod. Phys.* **68** 1259
[2] Hu M B, Jiang R and Wu Q S 2013 *Chin. Phys. B* **22** 066301
[3] Zhang N, Zhang S, Tan J J and Zhang W 2022 *Chin. Phys. B* **31** 024501
[4] Bester C S, Cox N, Zheng H and Behringer R P 2020 *Granular Matter* **22** 51
[5] Hou M, Peng Z, Liu R, Lu K and Chan C K 2005 *Phys. Rev. E* **72** 062301
[6] Katsuragi H and Durian D J 2007 *Nat. Phys.* **3** 420
[7] Ma H P, Lv Y J, Zheng N, Li L S and Shi Q F 2014 *Chin. Phys. Lett.* **31** 114501
[8] Constantino D J, Scheidemantal T J, Stone M B, Conger C, Klein K, Lohr M, Modig Z and Schiffer P 2008 *Phys. Rev. Lett.* **101** 108001
[9] Albert R, Pfeifer M A, Barabasi A L and Schiffer P 1999 *Phys. Rev. Lett.* **82** 205
[10] Pang Y and Liu C 2013 *Sci. China-Phys. Mech. Astron.* **56** 1428
[11] Kang W, Feng Y, Liu C and Blumenfeld R 2018 *Nat. Commun.* **9** 1101
[12] Herminghaus S 2005 *Adv. Phys.* **54** 221
[13] Mitarai N and Nori F 2006 *Adv. Phys.* **55** 1
[14] Marston J O, Vakarelski I U and Thoroddsen S T 2012 *Phys. Rev. E* **86** 020301
[15] Takita H and Sumita I 2013 *Phys. Rev. E* **88** 022203
[16] Artoni R, Loro G, Richard P, Gabrieli F and Santomaso A C 2019 *Powder Tech.* **356** 231
[17] Allen B and Kudrolli A 2019 *Phys. Rev. E* **100** 022901
[18] Nordstrom K N, Lim E, Harrington M and Losert W 2014 *Phys. Rev. Lett.* **112** 228002
[19] Guzman I L, Iskander M, Bless S and Qi C 2014 *Granular Matter* **16** 829
[20] Vella D 2015 *Annu. Rev. Fluid Mech.* **47** 115
[21] Twardos M and Dennin M 2005 *Granular Matter* **7** 91
[22] Zuo P, Liu J and Li S 2017 *Soft Matter* **13** 2315
[23] He W, Sun Y and Dinsmore A D 2020 *Soft Matter* **16** 2497
[24] Gallo Jr. A, Tavares F, Das R and Mishra H 2021 *Soft Matter* **17** 7628
[25] Jambon-Puillet E, Josserand C, and Protière S 2018 *Langmuir* **34** 4437
[26] Cicuta P and Vella D 2009 *Phys. Rev. Lett.* **102** 138302
[27] Petit P, Biance A, Lorenceau E and Planchette C 2016 *Phys. Rev. E* **93** 042802
[28] Lagarde A, Josserand C and Protière S 2019 *Soft Matter* **15** 5695
[29] Jones S G, Abbasi N, Ahuja A, Truong V and Tsai S S H 2015 *Phys. Fluids* **27** 072102
[30] Protière S, Josserand C, Aristoff J M, Stone H A and Abkarian M 2017 *Phys. Rev. Lett.* **118** 108001
[31] Ong X Y, Taylor S E and Ramaioli M 2019 *Langmuir* **35** 11150
[32] Hossain T and Rognon P 2020 *Phys. Rev. Fluids* **5** 054306
[33] Ozdemir O, Karakashev S I, Nguyen A V and Miller J D 2009 *Miner. Eng.* **22** 263
[34] Zhao C F, Kruyt N P and Millet O 2020 *Powder Technol.* **360** 622
[35] Keller J B 1998 *Phys. Fluids* **10** 3009
[36] Murray E J and Geddes J D 1987 *J. Geotech. Eng.* **113** 202
[37] Athani S and Rognon P 2021 *Granular Matter* **23** 67
[38] Jalali P, Zhao Y and Socolar J E S 2021 *Soft Matter* **17** 2832